Journal of
Synchrotron
Radiation

ISSN 0909-0495

Received 17 October 2006
Accepted 1 May 2007

X-ray beamlines for structural studies at the NSRRC superconducting wavelength shifter

Yen-Fang Song,[a]* Chien-Hung Chang,[a] Chin-Yen Liu,[a] Shih-Hung Chang,[a] U-Ser Jeng,[a] Ying-Huang Lai,[a] Din-Goa Liu,[a] Shih-Chun Chung,[a] King-Long Tsang,[a] Gung-Chian Yin,[a] Jyh-Fu Lee,[a] Hwo-Shuenn Sheu,[a] Mau-Tsu Tang,[a] Ching-Shiang Hwang,[a] Yeu-Kuang Hwu[b] and Keng S. Liang[a]

[a]National Synchrotron Radiation Research Center, Hsinchu 30076, Taiwan, and [b]Institute of Physics, Academia Sinica, Taipei 11529, Taiwan. E-mail: song@nsrrc.org.tw

Using a superconducting-wavelength-shifter X-ray source with a photon flux density of 10^{11}–10^{13} photons s^{-1} $mrad^{-1}$ (0.1% bandwidth)$^{-1}$ (200 mA)$^{-1}$ in the energy range 5–35 keV, three hard X-ray beamlines, BL01A, BL01B and BL01C, have been designed and constructed at the 1.5 GeV storage ring of the National Synchrotron Radiation Research Center (NSRRC). These have been designed for structure-related research using X-ray imaging, absorption, scattering and diffraction. The branch beamline BL01A, which has an unmonochromatized beam, is suitable for phase-contrast X-ray imaging with a spatial resolution of 1 μm and an imaging efficiency of one frame per 10 ms. The main beamline BL01B has 1:1 beam focusing and a medium energy resolution of $\sim 10^{-3}$. It has been designed for small-angle X-ray scattering and transmission X-ray microscopy, used, respectively, in anomalous scattering and nanophase-contrast imaging with 30 nm spatial resolution. Finally, the branch beamline BL01C, which features collimating and focusing mirrors and a double-crystal monochromator for a high energy resolution of $\sim 10^{-4}$, has been designed for X-ray absorption spectroscopy and high-resolution powder X-ray diffraction. These instruments, providing complementary tools for studying multiphase structures, have opened up a new research trend of integrated structural study at the NSRRC, especially in biology and materials. Examples illustrating the performances of the beamlines and the instruments installed are presented.

Keywords: superconducting wavelength shifter; hard X-ray beamline; structural study.

1. Introduction

Owing to their high penetration and potential for atomic resolution, hard X-rays are widely used for structure-related studies in materials, biology and many other fields. To increase the X-ray research activity at the National Synchrotron Radiation Research Center (NSRRC), we have installed a superconducting-wavelength-shifter (SWLS) insertion device (Hwang *et al.*, 2000, 2002) within the 1.5 GeV storage ring as a new X-ray source. This will supplement the existing tender X-ray beamline BL15B (Dann *et al.*, 1998) and the wiggler X-ray beamlines BL17A, BL17B and BL17C (Tsang *et al.*, 1995). The SWLS X-ray source, composed of three magnetic poles with a maximum magnetic field strength of 5 T, provides synchrotron radiation with a significantly higher critical photon energy of 7.5 keV, compared with the 2.1 keV of the bending magnet (BM) of 1.4 T. The new source delivers a photon flux density of 4.4×10^{12} photons s^{-1} $mrad^{-1}$ (0.1% bandwidth)$^{-1}$ (200 mA)$^{-1}$ at the critical photon energy. In the high-energy region of 15–35 keV, the flux of the new source is superior to that of the 1.8 T wiggler source (W20) of BL17 (which has thirteen 20 cm magnetic periods and a critical photon energy of 2.7 keV). The photon flux density of the SWLS, compared with that of W20 and BM, is shown in Fig. 1. Using a 20 mrad horizontal radiation fan of the new X-ray source, we have efficiently designed and constructed one main beamline BL01B, with the central 3 mrad of the radiation fan, and two branch beamlines BL01A and BL01C, with 1 mrad and 2 mrad radiation, respectively, from the two side wings.

Beamline BL01A, designed without optical components to preserve the coherence of the source, is suitable for white-beam X-ray imaging applications. The BL01B beamline, covering photon energies from 5 to 21 keV, is adequate for scattering-related instruments and hard X-ray microscopy. Finally, beamline BL01C, covering photon energies from 6 to 33 keV, is designed to accommodate two instruments for X-ray absorption spectroscopy (XAS) and powder X-ray diffraction (PXRD).

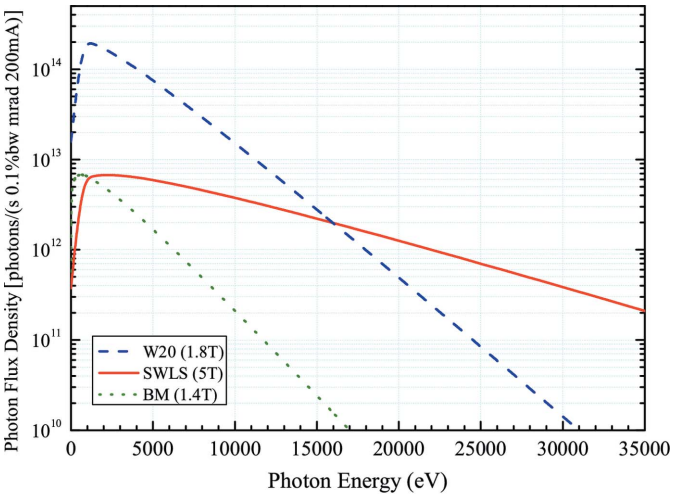

Figure 1
Photon flux density of the superconducting wavelength shifter, compared with that of the wiggler (W20) and bending magnet (BM).

These hard X-ray beamlines and end-stations, combined with the new SWLS X-ray source, have opened up new areas of research at the NSRRC in biology and materials. In this article we report on their design and performance for structure-related research.

2. Photon source

The SWLS insertion device, tightly fitted into a 61 cm space on the crowded 120 m circumference of the 1.5 GeV storage ring, consists of one central 5 T magnetic pole and two 3 T end-poles sited ±166 mm from the central magnetic pole. With the high magnetic field and an electron beam current of 200 mA, the SWLS is able to provide a high photon flux density of 10^{11}–10^{13} photons s^{-1} $mrad^{-1}$ (0.1% bandwidth)$^{-1}$ (200 mA)$^{-1}$ in the energy range 5–35 keV, with a critical photon energy of 7.5 keV. The corresponding total radiation power of the SWLS X-ray source amounts to 1.8 kW. The electron beam dimensions (close to those of the photon source) are 510 µm and 51 µm (in σ) in the horizontal and vertical directions, respectively, with corresponding beam divergences of 48 µrad and 20 µrad (in σ). The detailed source characteristics have been described previously (Hwang *et al.*, 2002).

In trading off beamline separation for photon flux, we have decided to use only 20 mrad of the radiation fan from the central magnetic pole. As a consequence, the radiation from the two end-poles cannot be blocked out efficiently before the end-stations of the two branch beamlines BL01A and BL01C, owing to the very small beamline separation. The ghost beam from the magnetic end-poles, about 6 mm from the main beam of the central magnetic pole, can, nevertheless, be blocked off with slits in the BL01A and BL01C end-stations located 24.5 m and 18 m away from the source, respectively.

3. Beamline design

Fig. 2 illustrates the geometry of beamlines BL01A, BL01B and BL01C at the NSRRC (Song *et al.*, 2004). Below, we describe in detail the designs of the three beamlines dictated by the characteristics of the SWLS X-ray source and the limited space available.

3.1. Beamline BL01A

Beamline BL01A collects 1 mrad from the right wing tip of the horizontal radiation fan of the SWLS X-ray source. With no optical component in the front-end section, the unmonochromatized beam is gated only by a water-cooled aperture. After passing through two 250 µm Be windows, the beam enters the hutch located 11.9 m from the source. The unmonochromatized beam fulfills the requirements of high penetration and high imaging speed for a microradiography system (detailed below). Since the sample area (also detailed below) of the imaging system is directly exposed to high-energy radiation, the shielding of this white-beam X-ray hutch is especially strengthened.

3.2. Beamline BL01B

Beamline BL01B takes the central 3 mrad of the horizontal radiation fan from the SWLS X-ray source. The beam is focused by a water-cooled toroidal focusing mirror FM(B) located at 15.5 m, with almost 1:1 focusing. The grazing incident angle of the beam on the Rh-coated FM(B) is chosen to be 3.2 mrad for 90% reflectivity at the designed cut-off energy of 21 keV (Hart & Berman, 1998). The X-ray beam is monochromated with a Ge(111) double-crystal monochromator DCM(B) located at 20.8 m. Taking into account the vertical divergence of the source, the error of the focusing mirror and the Darwin width of the Ge(111) crystals, the calculated energy resolution ($\Delta E/E$) (Hart & Berman, 1998) is 2.4×10^{-3} at 21 keV, and improves further with decreasing energy to 6.3×10^{-4} at 5 keV.

The beam size at the focus point, 30.2 m away from the X-ray source, was scanned using two sets of slits with 0.05 mm opening. The FWHM beam size, measured as 1.5 mm (H) × 0.5 mm (V), is larger than the source size of dimensions 1.2 mm × 0.12 mm. We attribute this non-ideal focusing to the manufacturing errors in the focusing mirror (6% in radius and 0.5 arcsec in slope error measured). With these errors taken into account, the beam size of 1.2 mm × 0.4 mm (FWHM) calculated using the ray-tracing program *SHADOW* (Welnak *et al.*, 1994) is close to that measured.

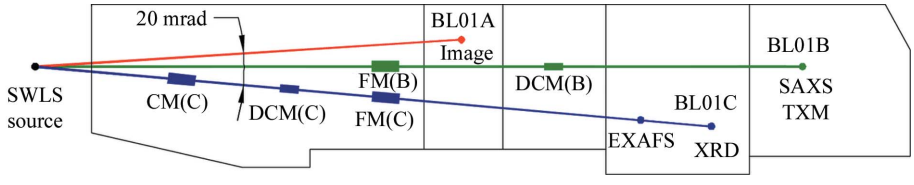

Figure 2
Top view of the optical layout of the three SWLS beamlines BL01A, BL01B and BL01C at the NSRRC, with the collimating mirror (CM), double-crystal monochromator (DCM) and focusing mirror (FM).

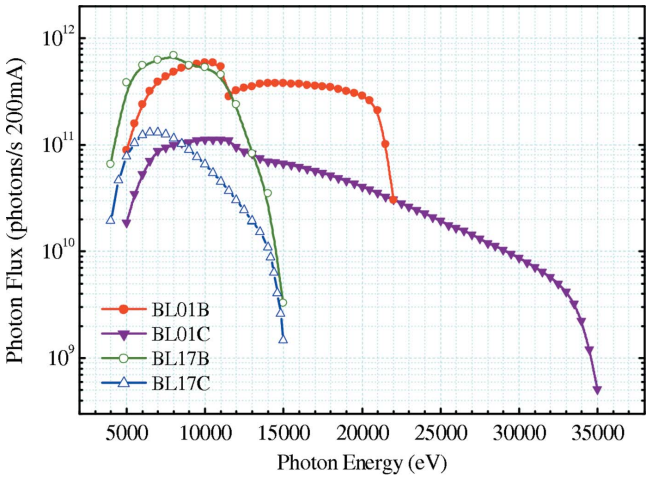

Figure 3
Measured photon flux at the focus positions of the beamlines BL01B and BL01C. Also shown are the fluxes of wiggler beamlines BL17B and BL17C.

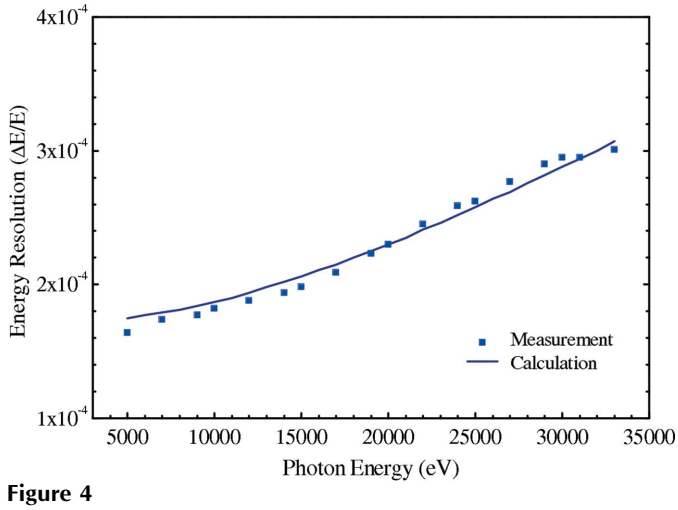

Figure 4
The measured energy resolution ($\Delta E/E$) of beamline BL01C closely matches the calculated values.

With a 15 cm-long ion chamber filled with 1×10^5 Pa nitrogen gas, we have measured the photon flux of the beam at the focal point, as shown in Fig. 3. In this figure the flux f_o is extracted from the ion chamber current using $f_o = IE_o/(EAeL)$, where I is the ion chamber current (in A), E_o (= 35 eV) is the energy dissipation per ion pair for nitrogen gas, E is the X-ray energy, A is the absorption of X-rays by nitrogen gas per 1 cm, e is the electron charge and L is the length of the ion chamber (Knoll, 1989). The measured photon flux, 1×10^{11}–6×10^{11} photons s^{-1} (200 mA)$^{-1}$ in the energy range 5–21 keV is consistent with that calculated using *SHADOW*. In the 15–21 keV high-energy region, the flux of BL01B is superior to that of the wiggler beamline BL17B by one to two orders of magnitude (see Fig. 3). The high-energy photons in this region are particularly useful in anomalous small-angle X-ray scattering (SAXS), X-ray absorption and diffraction for thick samples and/or materials containing elements of high atomic number, as detailed below.

3.3. Beamline BL01C

Beamline BL01C takes 2 mrad of radiation from the left wing tip of the horizontal radiation fan of the SWLS X-ray source. The beam is vertically collimated by a water-cooled mirror CM(C) located 11 m away from the source, then monochromated by a Si(111) double-crystal monochromator DCM(C) at 13.3 m. Subsequently, the beam is focused by a toroidal mirror FM(C) at 15.5 m, with the focus point at the sample position of the PXRD instrument situated 25.5 m away from the radiation source. With the collimating mirror placed before the DCM, the beam divergence from the radiation source is significantly reduced by a factor of ~10. Consequently, the energy resolution ($\Delta E/E$), estimated from the rocking curves of the DCM crystals, can be reduced to 1.7–3.0 $\times 10^{-4}$ in the energy range 6–33 keV (Fig. 4), which is close to that calculated using *SHADOW*, as shown in Fig. 4.

With a grazing incident angle of 2.5 mrad on the Pt-coated CM(C) and FM(C), the beam has a cut-off energy around 33 keV (90% reflectivity). The photon flux measured at the focus point (see Fig. 3) using an ion chamber, as described previously, is, however, lower than the calculated value by 50% in general, even though the intensity loss in the mirrors owing to the manufacturing errors are taken into account in the ray-tracing calculation. We have also calculated the slope change of the first DCM crystal (water-cooled) owing to a thermal loading of 60 W, using finite-element analysis (Song *et al.*, 2004). The additional slope error causes a 20% loss in the flux of higher-energy X-rays (30 keV), but does not affect the flux of low-energy X-rays very much (a few percent for 10 keV X-rays). Most likely, the slope errors of the CM and FM increase during the installation owing to bending stresses from the mirror-supporting frames, and contribute significantly to the loss of the flux mentioned.

4. Instrument performance

4.1. White-beam X-ray imaging system on BL01A

The white beam of the BL01A beamline is suitable for developing the phase-contrast X-ray imaging technique with high penetration and high imaging speed. Based on a similar principle to light microscopy, the white-beam X-ray imaging system installed on BL01A acts as a microprobe that can view fine internal structures of various objects, including biomaterials, with a resolution of 1 μm. With the high penetration power and high flux of the white beam, the imaging system can image thick and hard (high atomic number) samples, and has an imaging efficiency of one frame per 10 ms. Fig. 5(*a*) shows an X-ray image of an electron gun from a cathode radiation tube. The tungsten filament and the protective oxide layer can be distinguished clearly, even enclosed inside the cathode ray tube. Fig. 5(*b*) vividly shows the detailed internal structure of the head of a fruit fly, demonstrating that the phase-contrast X-ray imaging system installed can reveal the internal structures of biomaterials. This imaging system is expected to have many potential applications in life science at the NSRRC (Chen *et al.*, 2006).

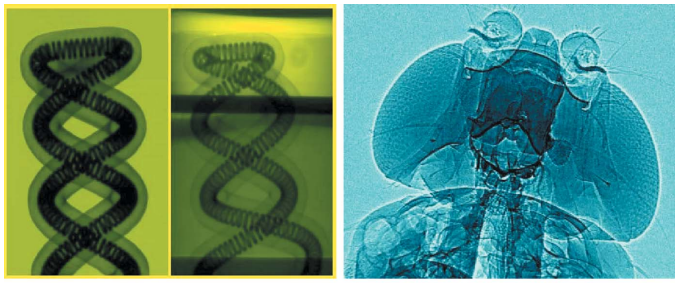

(*a*) (*b*)

Figure 5
(*a*) X-ray image of the electron gun of a cathode ray tube, before and after being enclosed in the case. (*b*) X-ray image of the head of a fruit fly.

4.2. SAXS and nanotransmission X-ray microscopy at BL01B

A SAXS instrument has been set up at the BL01B beamline for nanostructure research of, for instance, polymers and polymer composites, biomolecules in solutions, and nanoparticles (Lai *et al.*, 2005; Jeng *et al.*, 2005). The high flux and small beam divergence from the X-ray source are proven to be excellent for SAXS application. Fig. 6(*a*) shows the SAXS profiles taken for the Ag-behenate sample with an imaging plate, using two photon energies of 10.35 keV and 22.11 keV. The clearly discernible seventh-order peak at Q = 0.75 Å^{-1} is fitted with a Gaussian profile, demonstrating a good $\Delta Q/Q$ resolution of 0.46%. Here, Q is defined by $4\pi\sin(\theta/2)/\lambda$, where θ is the scattering angle and λ is the wavelength of the incident beam. With different combinations of beam wavelength and sample-to-detector distance, a measurable Q-range of 0.005–4 Å^{-1} can be covered by the SAXS instrument with a 20 cm × 20 cm area detector.

The wide energy spectrum of the SWLS X-ray source provides the possibility of resolving multiphase structures using anomalous SAXS. In Fig. 6(*b*) we show the anomalous SAXS for Pt–Ru nanoparticles embedded in fine carbon grains for fuel-cell applications, measured at one off-resonant energy, 10.353 keV, and two energies, 11.548 keV and 22.110 keV, close to the *L*- and *K*-absorption edges of Pt and Ru, respectively. With X-rays of 22.110 keV, the SAXS profile in the lower-Q region (Q < 0.07 Å^{-1}) decreases below that measured at the off-resonant energy, indicating that Ru dominates the shell structure of the Pt–Ru nanoparticles. On the other hand, with an X-ray energy near the L_3-absorption edge of Pt, the SAXS profile in the higher-Q region (Q > 0.15 Å^{-1}) falls below that measured at the off-resonant energy, demonstrating clearly that Pt dominates the core structure of the Pt–Ru nanoparticles.

Another instrument installed on the BL01B X-ray source is the nanotransmission X-ray microscope (TXM). In the energy range 8–11 keV, this instrument provides two-dimensional images and three-dimensional tomography with a spatial resolution of 30–60 nm. Equipped with Zernike-phase-contrast capability (Schmahl *et al.*, 1995; Schneider, 1998), the instrument can take images of light materials such as biological specimens. The spatial resolution δ of the microscope is given by $\delta = 0.9\Delta r/m$ (Yin, Song *et al.*, 2006), where Δr is the outermost width of the zone-plate, with the diffraction order

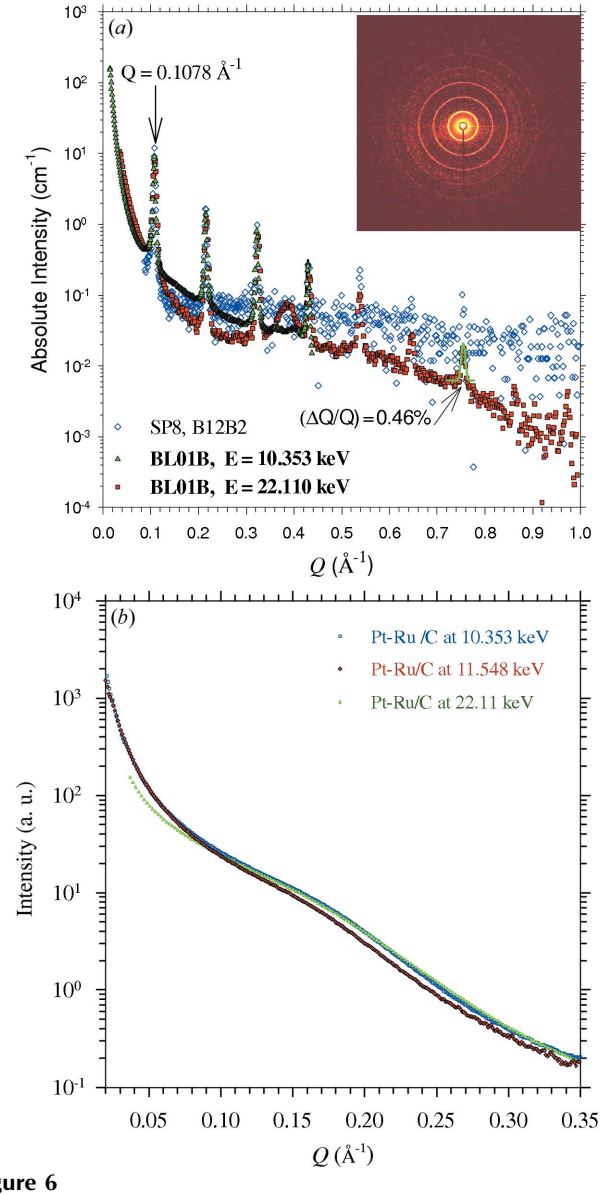

Figure 6
(*a*) SAXS data of Ag-behenate measured at 10.353 and 22.110 keV. Also shown are the data collected using the diffractometer at beamline BL12B2 (SPring-8) for comparison. (*b*) Anomalous SAXS data measured for the Pt–Ru bimetallic nanoparticles embedded in carbon black at three different X-ray energies, 10.353 keV, 11.548 keV and 22.11 keV.

m being an odd number. In principle, one can achieve m times better spatial resolution using the mth diffraction order at the expense of reducing focusing efficiency by $1/m^2$. The 50 nm outermost zone width of the present zone-plate can provide a nominal spatial resolution of either 45 nm or 15 nm, depending on the diffraction mode used (m = 1 or 3). The resolution of the microscope was tested by an electroplated gold Siemens star (fine line-width 30 nm) in the first-order and third-order diffraction modes, with corresponding fields of view of 15 µm × 15 µm and 5 µm × 5 µm. The finest discernible line-widths (imaged over several minutes and several tens of minutes for the two diffraction modes) illustrate the imaging resolution and efficiency of the instrument. In a modulation transfer function test with the third-order

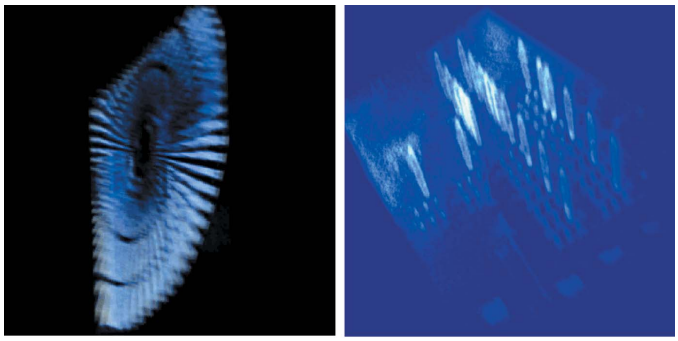

(*a*) (*b*)

Figure 7
(*a*) Three-dimensional tomography of a gold spoke pattern, taken with a resolution of ~60 nm and an imaged volume of 15 μm × 15 μm × 1 μm. (*b*) Three-dimensional tomography of an integrated circuit (IC), taken with an imaged volume of 12.5 μm × 7.9 μm × 5.2 μm, clearly showing the hollows at the center of the IC plugs (bright rods).

diffraction mode, a spatial resolution of 30 nm is achieved. The phase contrast of a phase ring is measured to be 12%, with a plastic zone-plate of thickness 1 μm and an absorption contrast of 0.01%, using 8 keV X-rays.

The tomography of the microscope was tested with an electroplated gold spoke pattern and an integrated circuit (IC) provided by PSC (Yin, Tang *et al.*, 2006). The tomography of the gold spokes shown in Fig. 7(*a*) is reconstructed based on the 141 sequential image frames taken over several hours, in first-order diffraction mode with the azimuth angle rotating from −70° to 70°. The corresponding spatial resolution of the gold spoke pattern is estimated to be ~60 nm. In principle, one can take more images for a better image reconstruction to satisfy the oversampling theorem when the instrument time is not a concern. In another example shown in Fig. 7(*b*) for an IC sample, the buried hollows in tungsten plugs, related to an essential failure mode of the IC, can be clearly unveiled in the three-dimensional reconstructed images.

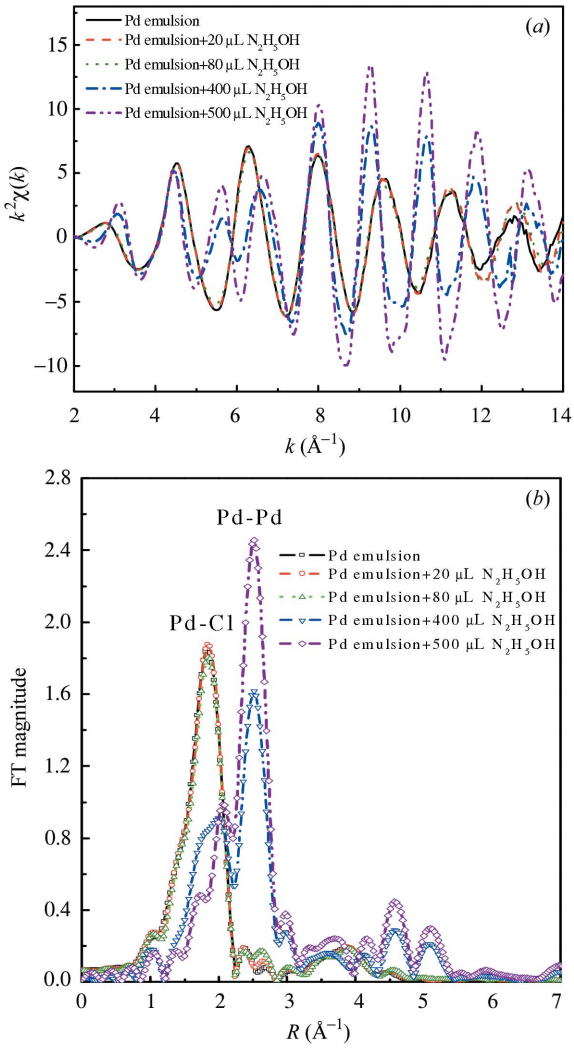

Figure 8
(*a*) Pd *K*-edge EXAFS data after k^2-weighting. (*b*) Radial distribution functions of the Pd atoms in different environments.

4.3. X-ray absorption and powder X-ray diffraction at BL01C

In the end-station of BL01C, two instruments for X-ray absorption spectroscopy and powder X-ray diffraction, emphasizing high-energy X-ray (15–35 keV) applications, have been installed in series and used on an interchange basis. To examine the performance of the XAS instrument, we have measured X-ray absorption spectra at the Pd *K*-edge (24.350 keV) for a micro-emulsion system, containing K_2PdCl_6 precursors and the reducing agent N_2H_5OH for the formation of Pd clusters. The XAS spectra measured, which have excellent signal-to-noise ratio, are converted to useful extended X-ray absorption fine-structure (EXAFS) data covering a wide *k*-region up to 14 Å^{-1}. Fig. 8(*a*) shows the k^2-weighted ($k = 2\pi/\lambda$) EXAFS data for the microemulsion system with different concentrations of the reducing agent. The radial distribution functions obtained from the Fourier transformation of the corresponding EXAFS data (Fig. 8*b*) illustrate an increase in Pd–Pd peak height at the expense of the Pd–Cl peak intensity, which reveals that the addition of the reducing agent leads to a progressive reduction of the Pd species to a metallic state.

In terms of the performance of the X-ray diffraction (XRD) instrument, the diffraction pattern measured for a $KNiF_3$ powder with 28.0 keV X-rays (Fig. 9*a*) demonstrates the high-quality data (wide *Q*-range and low background) which can be recorded. The PXRD pattern was obtained using an imaging plate with a curvature radius of 280 mm, in a typical 10 min exposure time. For comparison, the XRD pattern for the same sample measured at beamline 2 of SPring-8, with a similar set-up and a similar data quality, is also shown (Fig. 9*a*). Fig. 9(*b*) presents a high-resolution powder diffraction pattern of a quartz sample collected with 12 keV X-rays, using the same set-up as the previous sample. As shown in the insert of Fig. 9(*b*), the packed fingerprint pattern of (122), (203) and (031) peaks of the quartz sample can still be resolved from the wide-*Q*-range XRD pattern. Currently, several studies using the advantages of the high-energy high-resolution XRD instrument are underway, including nanosize materials XRD, *in situ* measurement of Li-ion battery electrodes during

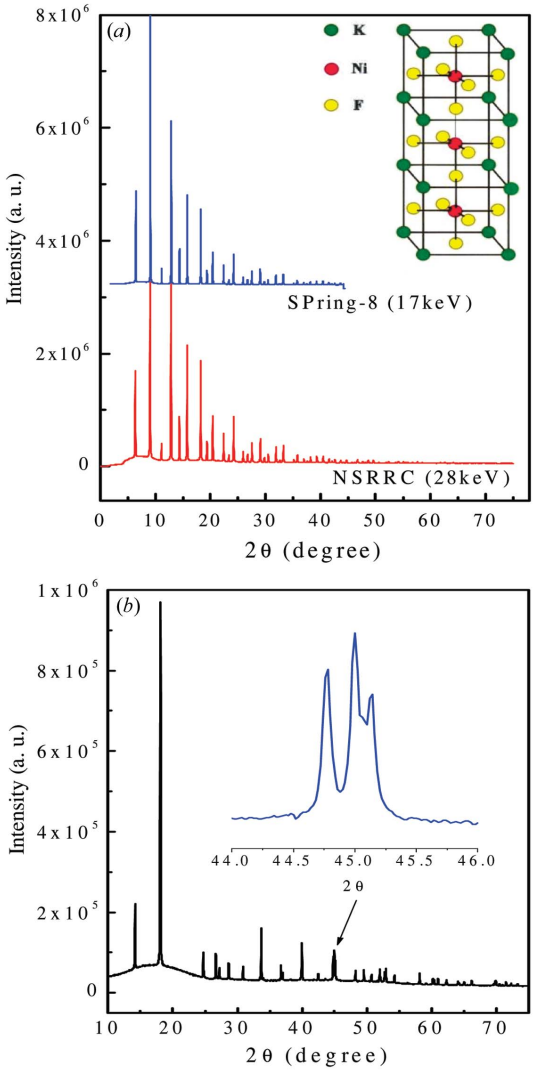

Figure 9
(*a*) X-ray diffraction patterns of $KNiF_3$ measured at the NSRRC (28 keV) and SPring-8 (17 keV). The insert shows the crystal model of $KNiF_3$. (*b*) Powder diffraction pattern for a quartz sample (NSRRC, 12 keV). The insert shows an expanded view of the well resolved fingerprint pattern (122), (203) and (031) of quartz.

charging–discharging cycles (Lin *et al.*, 2005; Chan *et al.*, 2006), high-pressure XRD with a diamond-anvil cell, and temperature-dependent non-ambient crystallography (Her *et al.*, 2006).

5. Concluding remarks

With the new SWLS X-ray source, we have delivered three hard X-ray beamlines for fast X-ray imaging, X-ray scattering, nano X-ray microscopy, X-ray absorption and powder X-ray diffraction applications. The characteristics and performances of the beamlines and the instruments are illustrated by the preliminary results of several systems. These instruments are currently used for a variety of projects, including phase-contrast X-ray microscopy of metal-label cells, *in situ* XRD/XAS investigation of cathode materials in Li-ion batteries, and a SAXS/XRD/XAS study of the core–shell structure of Pt–Ru bimetallic nanoparticles. It is expected that these instruments will be able to complement each other for systems of hierarchical structures over a wide length scale, ranging from atomic, through nano and meso, to micrometer sizes. The work presented here may provide a good example for small storage rings in developing X-ray applications.

The authors thank all NSRRC staff, especially those in the Beamline Group, as well as Dr Chi-Chang Kao and Dr Chia-Hung Hsu for their kind assistance.

References

Chan, H. W., Duh, J. G. & Sheu, H. S. (2006). *J. Electrochem. Soc.* **153**, A1533–A1538.
Chen, J. Y., Bottjer, D. J., Davidson, E. H., Dornbos, S. W., Gai, X., Yang, Y. H., Li, C. W., Li, G., Wang, X. W., Xian, D. C., Wu, H. J., Hwu, Y. & Tafforeau, P. (2006). *Science*, **312**, 1644–1646.
Dann, T. E., Chung, S. C., Huang, L. J., Juang, J. M., Chen, C. I. & Tsang, K. L. (1998). *J. Synchrotron Rad.* **5**, 664–666.
Hart, M. & Berman, L. (1998). *Acta Cryst.* A**54**, 850–858.
Her, J. L., Liu, H. L., Shen, C. H., Liu, R. S. & Sheu, H. S. (2006). *J. Appl. Phys.* **99**, 013905.
Hwang, C. S., Chang, P. C., Chang, C. H., Hsial, F. Z. & Chen, C. T. (2000). *IEEE Trans. Appl. Superconduct.* **10**, 503–506.
Hwang, C. S., Wang, B., Wahrer, R., Chen, H. H., Lin, F. Y., Fan, T. C. & Chen, C. T. (2002). *IEEE Trans. Appl. Superconduct.* **12**, 686–690.
Jeng, U., Hsu, C. H., Sun, Y. S., Lai, Y. H., Chung, W. T., Sheu, H. S., Lee, H. Y., Song, Y. F., Liang, K. S. & Lin, T. L. (2005). *Macromol. Res.* **13**, 506–513.
Knoll, G. F. (1989). *Radiation Detection and Measurement*, p. 132. New York: John Wiley.
Lai, Y. H., Sun, Y. S., Jeng, U., Huang, Y. S., Song, Y. F., Dronyak, R., Tsang, K. L. & Liang, K. S. (2005). *Nucl. Instrum. Methods B*, **238**, 205–213.
Lin, Y. M., Wu, H. C., Guo, Z. Z., Yang, M. H., Chen, H. M., Sheu, H. S. & Wu, N. L. (2005). *J. Electrochem. Soc.* **152**, A1526–A1532.
Schmahl, G., Rudolph, D., Guttmann, P., Schneider, G., Thieme, J. & Niemann, B. (1995). *Rev. Sci. Instrum.* **66**, 1282–1286.
Schneider, G. (1998). *Ultramicroscopy*, **75**, 85–104.
Song, Y. F., Chang, C. H., Liu, C. Y., Huang, L. R., Chang, S. H., Tseng, P. C., Chuang, J. M., Chung, S. C., Lee, J. F., Tsang, K. L. & Liang, K. S. (2004). *Eighth International Conference on Synchrotron Radiation Instrumentation*, *AIP Conference Proceedings 705*, pp. 412–415. Melville, NY: AIP Press.
Tsang, K. L., Lee, C. H., Jean, Y. C., Dann, T. E., Chen, J. R., D'Amico, K. L. & Oversluizen, T. (1995). *Rev. Sci. Instrum.* **66**, 1812–1814.
Welnak, C., Chen, G. C. & Cerrina, F. (1994). *Nucl. Instrum. Methods A*, **347**, 344–347.
Yin, G. C., Song, Y. F., Tang, M. T., Chen, F. R., Liang, K. S., Duewer, F. W., Feser, M., Yun, W. & Shieh, H. P. (2006). *Appl. Phys. Lett.* **89**, 221122.
Yin, G. C., Tang, M. T., Song, Y. F., Chen, F. R., Liang, K. S., Duewer, F. W., Yun, W., Ko, C. H. & Shieh, H. P. (2006). *Appl. Phys. Lett.* **88**, 241115.